**Steel and Composite Structures**, *Vol. 25, No. 6 (2017) 705-716*
DOI: https://doi.org/10.12989/scs.2017.25.6.705


# Behavior of headed shear stud connectors subjected to cyclic loading

Fa-xing Ding[1], Guo-an Yin[*1], Hai-bo Wang[1], Liping Wang[1] and Qiang Guo[1,2]

[1]*School of Civil Engineering, Central South University, Changsha, Hunan Province, 410075, P.R. China*
[2]*CRRC CONSTRUCTION ENGRG. CO., LTD., P.R. China*

(*Received May 1, 2017, Revised August 29, 2017, Accepted September 15, 2017*)

**Abstract.** The objective of this study is to investigate the actual behavior of studs in structures under earthquake load through laboratory tests and numerical simulation. A test program including eighteen specimens was devised with consideration of different concrete strengths and stud diameters. Six of specimens were subjected to monotonically increasing loading while the others were subjected to cyclic loading. Mechanical behavior including the failure mechanism, load-slip relationship, stiffness degradation, energy dissipation and the damage accumulation was obtained from the test results. An accurate numerical model based on the ABAQUS software was developed and validated against the test results. The results obtained from the finite element (FE) model matched well with the experimental results. Furthermore, based on the experimental and numerical data, the design formulas for expressing the skeleton curve were proposed and the simplified hysteretic model of load versus displacement was then established. It is demonstrated that the proposed formulas and simplified hysteretic model have a good match with the test results.

**Keywords:** headed stud shear connector; push-off test; cyclic loading; energy dissipation; finite element model

## 1. Introduction

In recent decades, steel-concrete composite structures, with the benefits of combining the advantages of their components, have been widespread in buildings and bridges (Debski *et al*. 2016, Uy 2003, Wiese *et al*. 2011). As an important component of composite beams, the shear connectors are used to transfer the tangential shear force at the steel-concrete composite interface (Fang *et al*. 2016, Liu *et al*. 2016). Among the different types of shear connectors, headed shear connector is most commonly used in steel-concrete composite constructions, due to its economic efficiency and fast construction speed. Hence, a lot of research has been done to study the behavior of studs.

Prakash *et al*. (2012) conducted experiments on high strength steel (HSS) stud connected steel-concrete composite girds under monotonic, quasi-static and non-reversal cyclic loading. The results showed that this composite girds have a good ductility and use of HSS studs will reduce stud numbers for given loading. Wang *et al*. (2017) proposed a residual strength degradation model for stud shear connectors under fatigue loads and this model can better describe the strength degradation law of stud connectors. Wang *et al*. (2014) investigated the fatigue behavior of steel-concrete composite beams and studs, and proposed an effectively calculation method for the deflection of steel-concrete composite beam. It was found that the equation in AASHTO (American Association of State Highway and Transportation Officials) was the safest equation to predict the fatigue life of stud in practical design. Ju *et al*. (2015) studied the effect of axial uplift force of studs on steel-concrete composite structures based on the stud uplift tests, and gave the detail test results in the fatigue strength and the fatigue S-N curve of studs. Hanswille *et al*. (2007a, 2007b) carried out the experimental and analytical study on the resistance of headed studs subjected to fatigue loading. The results show that the crack initiation at the stud foot at 10%-15% of the fatigue life caused an early reduction of the static strength of studs, and the linear damage accumulation hypothesis presented by Palmgren and Miner on which the present design codes are based do not describe the real behavior of studs.

The seismic performance of studs under cyclic loading has not been well studied yet (experimentally in particular), although this topic is highly important for the application of composite beams in seismic regions. Gattesco *et al*. (1996) carried out a preliminary study on the stud shear connectors subjected to cyclic loading, but the detailed hysteresis rules, strength and stiffness degradation and energy dissipation were not provided. Therefore, this study will focus on this point. In this work, the static and seismic behaviors of studs are presented based on the results of both experimental investigation and numerical simulation. The experimental work consists of six push-out tests and twelve cyclic loading tests. Based on the test results, the effect of stud diameter and concrete strength on the load-slip relationship, ultimate shear capacity, stiffness and strength degradation as well as energy dissipation was evaluated. Precise finite element (FE) models were further established and verified against the experiment data. Based on both experimental and numerical results, design formulas for determining the skeleton curves and simplified hysteretic model of load ($P$) versus displacement ($\Delta$) were proposed. The proposed formulas and simplified hysteretic model have a good

∗Corresponding author, Ph.D.
E-mail: 124812242@csu.edu.cn


http://www.techno-press.org/?journal=scs&subpage=6 ISSN: 1229-9367 (Print), 1598-6233 (Online)

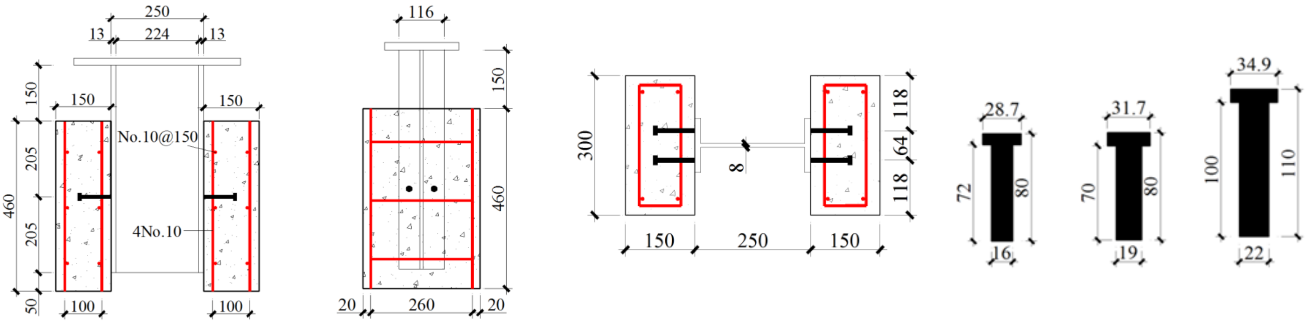


(a) Front view (b) Side view (c) Top view (d) Different studs

Fig. 1 Detail of the specimens; units: mm

Table 1 Key information of specimens

| Specimens | Concrete slab | | | Stud | | $f_{cu}$/ MPa | Geometric reinforcement ratio | |
|---|---|---|---|---|---|---|---|---|
| | $L$/mm | $B$/mm | $H$/mm | $d$/mm | $h$/mm | | $\rho_l$/% | $\rho_t$/% |
| FP1 or CL1-1, 2 | 460 | 300 | 150 | 16 | 80 | 33.1 | 0.70 | 0.91 |
| FP2 or CL2-1,2 | 460 | 300 | 150 | 19 | 80 | 33.1 | 0.70 | 0.91 |
| FP3 or CL3-1,2 | 460 | 300 | 150 | 22 | 110 | 33.1 | 0.70 | 0.91 |
| FP4 or CL4-1,2 | 460 | 300 | 150 | 16 | 80 | 47.8 | 0.70 | 0.91 |
| FP5 or CL5-1,2 | 460 | 300 | 150 | 19 | 80 | 47.8 | 0.70 | 0.91 |
| FP6 or CL6-1,2 | 460 | 300 | 150 | 22 | 110 | 47.8 | 0.70 | 0.91 |

Table 2 Material properties of steel, concrete and stud

| Material | $f_{cu}$ or $f_y$/MPa | $f_u$/MPa | $E_s$ or $E_c$/GPa | $A$/% | $v_s$ or $v_c$ |
|---|---|---|---|---|---|
| C30 | 33.1 | NA | 30.5 | NA | 0.20 |
| C50 | 47.8 | NA | 34.5 | NA | 0.20 |
| I25a steel | 313.1 | 446.6 | 206.0 | 45.3 | 0.285 |
| No. 10 bars | 253.4 | 380.7 | 206.0 | 32.5 | 0.285 |
| $\varphi$16 Stud | 380.0 | 480.0 | 206.0 | 17.0 | 0.30 |
| $\varphi$19 Stud | 380.0 | 480.0 | 206.0 | 17.0 | 0.30 |
| $\varphi$22 Stud | 380.0 | 475.0 | 206.0 | 17.0 | 0.30 |

Table 3 Mixtures and properties of concrete

| Material | Cement (kg/m$^3$) | Coarse aggregate (kg/m$^3$) | Fine aggregate (kg/m$^3$) | Water (kg/m$^3$) | Water reducer (kg/m$^3$) |
|---|---|---|---|---|---|
| C30 | 461 | 1252 | 512 | 175 | 0 |
| C50 | 450 | 1210 | 660 | 150 | 1.125 |

match with the test results.

## 2. Experimental research

### 2.1 Test specimens

In order to examine the static and seismic behavior of headed stud shear connectors, eighteen specimens were designed and fabricated according to the standard push-out test specimen in code BS 5400-5. The specimens were divided into two groups. One group (six specimens), denoted as FP1 to FP6 in group 1, were designed for push-off tests and the others (twelve specimens), designated as CL1 to CL6, were used for cyclic loading tests. There is a repeat specimen (CL1-2 to CL6-2) for each cyclic loading test.

The test specimen shown in Fig. 1 consists of a steel beam ($h_b$×$b_f$×$t_f$×$t_w$=250×116×13×8 mm, I25a for short), two concrete slab attached to the flanges of the steel beam with dimension of 460 mm in length, 300 mm in width, and 150 mm in thickness for each slab, and two headed stud shear connectors attached to each flange with shank diameter ($d$) of 16 mm (nominal length $h$=80 mm) or 19 mm (nominal length $h$=80 mm) or 22 mm (nominal length $h$=110 mm). Studs weld with the steel beam by completely penetration butt weld. A summary of specimen information is listed in Table 1. $f_{cu}$ is the cubic compressive strength of concrete. $\rho_l$ is the longitudinal steel ratio and $\rho_t$ is the transverse reinforcement ratio.

### 2.2 Materials

Q235 steel with nominal yield strength of 235 MPa was used for I25a steel beam. Hot-rolled ribbed bars (HRB) with nominal yield strength of 235 MPa and diameter of 10 mm were used as reinforcing bars spaced by 150 mm. Three types of headed stud shear connectors with different diameter (see Fig. 1(d)) were used to transfer the shear force between the steel beam and concrete slab. The type of studs was grade 4.6. Tensile coupling tests were carried out for the structural steel and reinforcing bars according to GB/T 228-2010 before the test and the results are presented in Table 2.

Two types of concrete with nominal compressive cube strength of 30 MPa (C30) and 50 MPa (C50) were used in this study. Silica based sand and crushed carbonate stone were used as fine aggregate and coarse aggregate, respectively. The mix proportion is summarized in Table 3. The material properties of the concrete obtained by standard cubes (150×150×150 mm) after 28 days of curing according to the Chinese standard GB/T 50081-2016 and Eurocode 4 are shown in Table 2.

### 2.3 Experimental setup and loading procedure

Fig. 2 shows a schematic view of the test setup. The test specimen was fastened to the strong floor through a steel

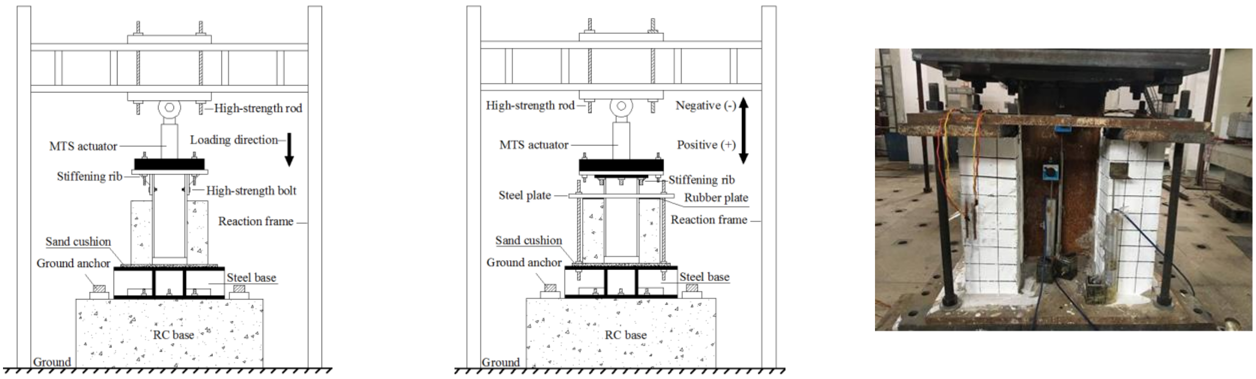


(a) Push-off test (b) Cyclic loading test (c) Experimental setup photograph

Fig. 2 Test setup

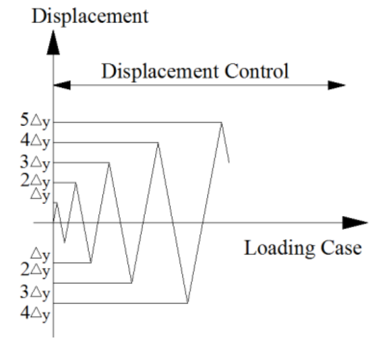


Fig. 3 Loading history in cyclic loading test

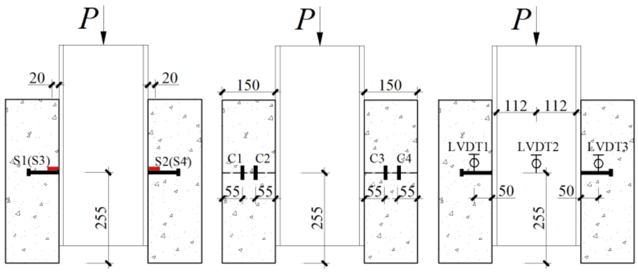


(a) Strain in studs (b) Strain in RC slab (c) LVDTs arrangement

Fig. 4 Instrumentation of strain gauges and LVDTs; units: mm

base and a reinforced concrete (RC) base. The specimens were tested in hydraulic testing machine with a capacity of 500 kN and a stroke of ±100 mm. In the cyclic loading tests, additional steel and rubber plates were placed on the top of RC slabs and connected with the steel base through high-strength rods, as shown in Fig. 2(b), in order to limit the upward displacement of RC slabs.

A steel plate with dimension of 380 mm in length, 260 mm in width, and 20 mm in thickness was connected with a 30 mm thickness steel plate by six high-strength bolts to ensure the stability. After the instrumentation arrangement was finished, the vertical load (approximately 30% of the ultimate load $P_u$) was applied to examine the test setup and instrumentation. Preloading was conducted for 5 mins and then released to zero. Foundation bolts were tightened again. Testing was then started under multistep loading schemes.

A load-control mode with multistep loading scheme was employed in the push-out tests. The load was applied in increments of 20 kN up to $0.5P_u$, the load was then decreased to 10 kN up to $0.8P_u$, the last loading step was 5 kN until the vertical load could not be sustained, the test was terminated.

A displacement-control mode with multistep loading scheme was taken in the cyclic loading tests. The end of the steel beam was subjected to the cyclic load at the level of 1Δ, 2Δ, 3Δ, 4Δ….respectively, where Δ was equal to 0.5 mm. Only one cycle was imposed at each displacement level, as shown in Fig. 3. The test was completed until the load decreased below 85% of the maximum measure load capacity of the test specimen or the specimen appeared the abrupt failure.

Strain gauges were bonded to each of headed stud shear connector bottom (e.g., S1) and the surface of the concrete slab (e.g., C1) to study the strain development. Several linear variable differential transformers (LVDTs) were used to measure the longitudinal slip of stud. The arrangement of strain gauges and LVDTs is shown in Fig. 4.

## 3. Test results

### 3.1 Load-displacement relationship

For push-out specimens, the load-displacement curves (see Fig. 5) consisted of two parts, ascending and descending part. The ascending section could be separated into elastic and plastic parts. In the elastic part, the curves showed almost linear relationship. In the plastic part, the displacement increased rapidly and the stiffness reduced continuously. Table 4 summarizes the characteristic load and slip for a single stud. $P_u^T$, $P_f^T$ is defined as the ultimate and failure load, and $s_u^T$ and $s_f^T$ is the corresponding displacement. $P_6$ is defined as the load when the characteristic slip was 6 mm. From Table 4, the increasing of concrete strength and stud diameter increased the ultimate shear capacity. For instance, the ultimate load of specimens FP2 and FP3 increased by 29.3% and 44.2% by comparing with specimen FP1, respectively; ultimate load of specimens FP1, FP2 and FP3 increased by 28.3%, 15.0% and 32.7% by comparing with the corresponding specimens


(a) Specimens FP1 to FP3 (b) Specimens FP4 to FP6

Fig. 5 Load-displacement curves of push-out tests

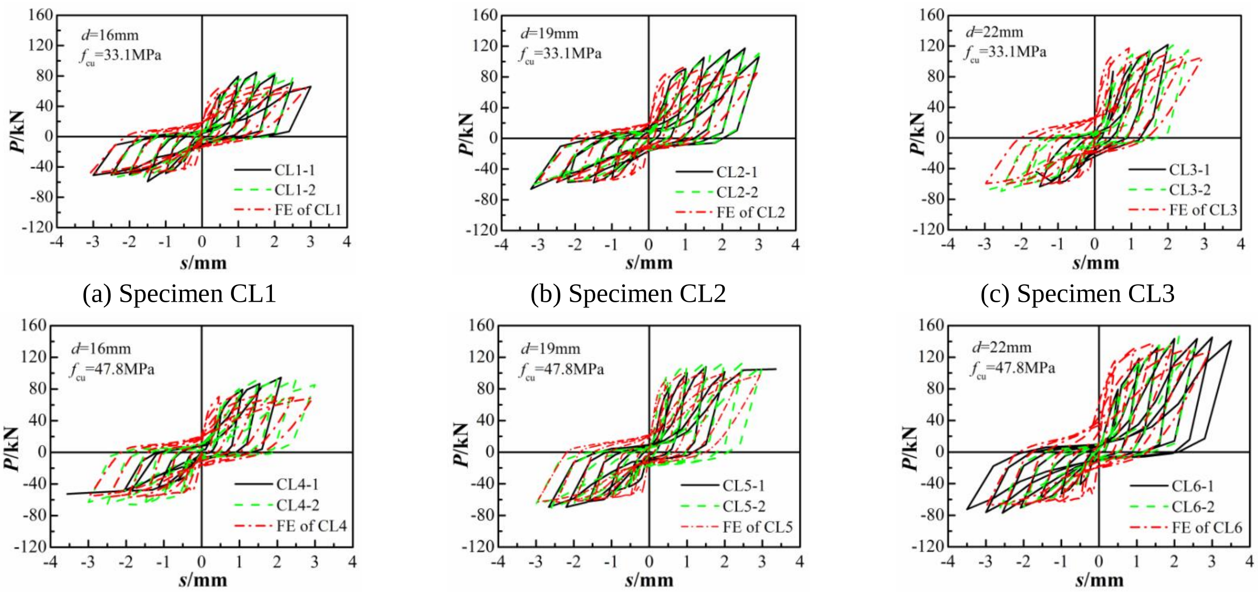


(a) Specimen CL1 (b) Specimen CL2 (c) Specimen CL3

(d) Specimen CL4 (e) Specimen CL5 (f) Specimen CL6

Fig. 6 Load-displacement hysteretic curves of cyclic loading tests

Table 4 Test results in push-out test

| Specimens | $d$/ mm | Material | $P_u^T$/ kN | $s_u^T$/ mm | $P_f^T$/ kN | $s_f^T$/ mm | $P_f^T$/ $P_u^T$ | $P_6$/ kN | Failure mode |
|---|---|---|---|---|---|---|---|---|---|
| FP1 | 16 | | 81.0 | 4.18 | 32.85 | 5.40 | 0.41 | NA | Shank failure |
| FP2 | 19 | C30 | 104.7 | 3.16 | 42.00 | 7.21 | 0.40 | 94.7 | Shank failure |
| FP3 | 22 | | 116.8 | 2.21 | 38.75 | 3.58 | 0.33 | NA | Concrete failure |
| FP4 | 16 | | 103.9 | 1.90 | 71.25 | 4.87 | 0.69 | NA | Shank failure |
| FP5 | 19 | C50 | 120.4 | 1.71 | 110.25 | 2.03 | 0.92 | NA | Shank failure |
| FP6 | 22 | | 155.0 | 1.55 | 153.75 | 1.97 | 0.99 | NA | Shank failure |

Table 5 Test results in cyclic loading test

| Number | Specimen | $d$/mm | $f_{cu}$/MPa | $P_u^+$/kN | $P_u^-$/kN | Failure mode |
|---|---|---|---|---|---|---|
| 1 | CL1-1 | 16 | 33.1 | 85.25 | -59.25 | Stud failure |
| | CL1-2 | | | 86 | -54.5 | Stud failure |
| 2 | CL2-1 | 19 | 33.1 | 117.25 | -66 | Concrete failure |
| | CL2-2 | | | 115 | -61 | Concrete failure |
| 3 | CL3-1 | 22 | 33.1 | 122 | -63.75 | Concrete failure |
| | CL3-2 | | | 121.25 | -69.5 | Concrete failure |
| 4 | CL4-1 | 16 | 47.8 | 93.5 | -66 | Stud failure |
| | CL4-2 | | | 94.5 | -52.5 | Stud failure |
| 5 | CL5-1 | 19 | 47.8 | 107.75 | -69.5 | Stud failure |
| | CL5-2 | | | 114.5 | -70.25 | Concrete failure |
| 6 | CL6-1 | 22 | 47.8 | 145.25 | -77 | Concrete failure |
| | CL6-2 | | | 147 | -71.75 | Concrete failure |

FP4, FP5 and FP6, respectively.

For cyclic loading specimens, it was observed from Fig. 6 that all of the hysteresis curve shape was full and basically belonged to reversed S shape with obvious pinching phenomenon. This was mainly because of concrete crack, deformation of stud, and the formation of the microvoid between the stud and concrete slab under cyclic loading. Table 5 summarizes the characteristic load in cyclic loading tests and Fig. 7 shows the skeleton load-displacement curves. It can be found that all skeleton curves had gentle descending stage. As shown in Fig. 7 and Table 5, specimens CL3 and CL6 had higher ultimate shear capacity than other specimens since specimen CL3 had

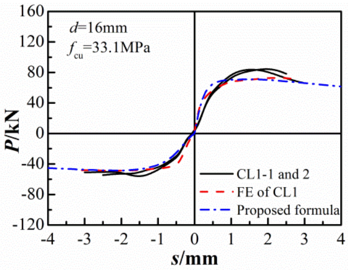


(a) Specimen CL1

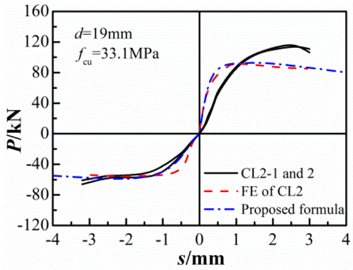


(b) Specimen CL2

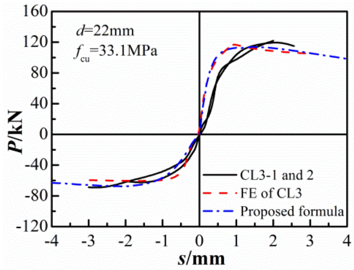


(c) Specimen CL3

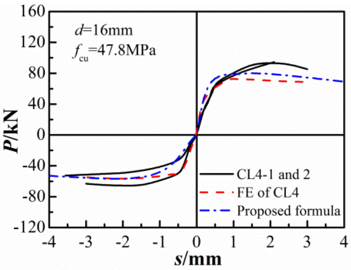


(d) Specimen CL4

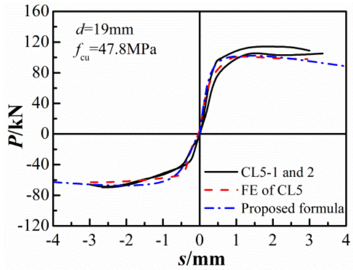


(e) Specimen CL5

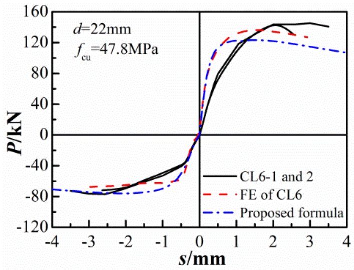


(f) Specimen CL6

Fig. 7 Skeleton curves of cyclic loading tests


(a) Stud failure

(b) Concrete failure

Fig. 8 Failure modes

bigger stud diameter than specimens CL1 and CL2, and specimen CL6 had higher concrete strength than specimens CL4 and CL5. However, the vertical displacement of specimen CL3 was less than the other two specimens due to the concrete failure. The area surrounded by hysteretic curve of specimen CL6 was greater than other specimens, indicating a higher concrete strength provides greater energy dissipation.

### *3.2 Failure modes*

As expected, stud shank fracture (see Fig. 8(a)) occurred at the stud bottom near weld toes was the typical failure mode in the push-off test. No weld damage happened in all test specimens. The failure modes of the push-out specimens are summarized in Table 4. For specimens FP1, FP2 and FP3, crack firstly initiated near the location of studs, and then distributed and propagated on the concrete slab when the load reached 70%-80% of the maximum load. The load value of specimen FP3 dropped rapidly after the maximum load due to the concrete crushed. However, specimens FP1 and FP2 could sustain load even after reaching the ultimate load and the tests were terminated owing to the abrupt failure of studs. Specimens FP4, FP5 and FP6 had the similar phenomenon except no cracks occurred

For cyclic loading specimens, similar phenomenon was observed during the loading process. Horizontal cracks firstly appeared on the surface of RC slabs at the initial stage of loading and the cracks developed with the increasing load. Abrupt failure of stud created the termination of trial for specimens CL1 and CL4 due to the smaller stud diameter. Meanwhile, concrete crushed were the primary causes, resulting in the failure of the other specimens. A large number of vertical and slant cracks were observed on the upper surface of RC slab for all cyclic loading specimens after the test. The failure modes of the cyclic loading specimens are summarized in Table 5.

### *3.3 Stiffness degradation*

The ring stiffness method (Ding *et al*. 2017) was used to analyze the stiffness degeneration, which can be expressed as

$$K_i = \frac{\sum_{i=1}^{m} P_j^i}{\sum_{i=1}^{m} \Delta_j^i} \tag{1}$$

where $K_i$ is the ring stiffness; $P^i_j$ is the peak load for the $i^{th}$ loading cycle at the $j^{th}$ displacement ductility ratio; $\Delta^i_j$ is the corresponding peak displacement for the $i^{th}$ loading cycle at the $j^{th}$ displacement ductility ratio; $m$ is the cycle number.

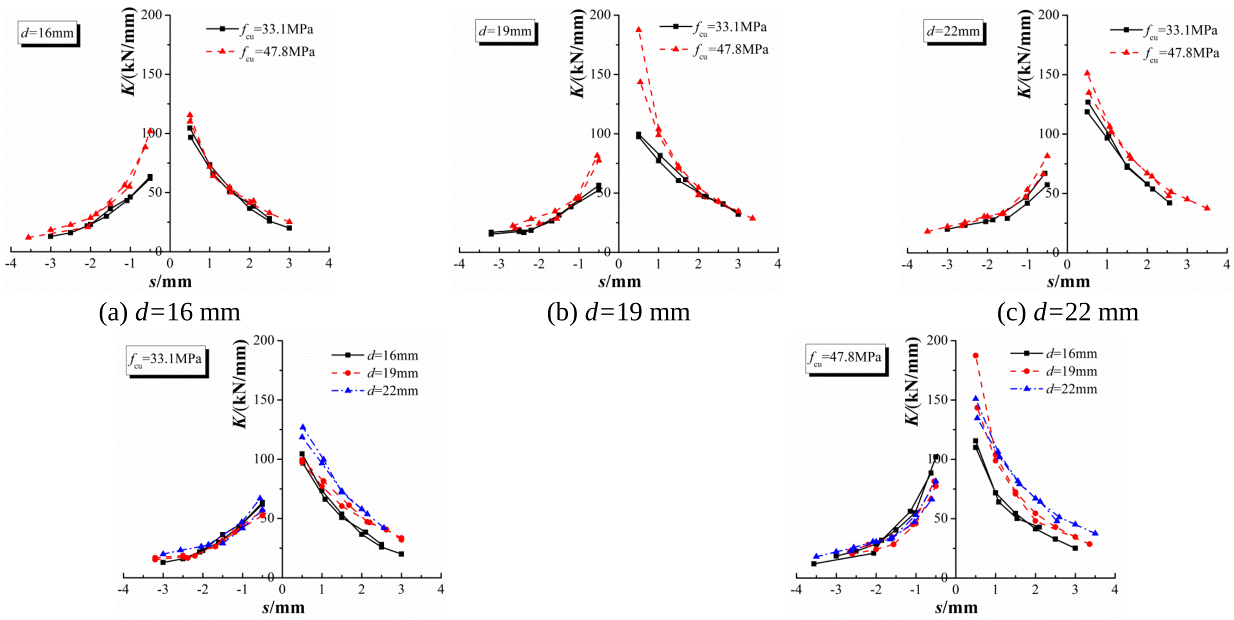


(a) $d$=16 mm (b) $d$=19 mm (c) $d$=22 mm

(d) $f_{cu}$=33.1 MPa (e) $f_{cu}$=47.8 MPa

Fig. 9 Stiffness degradation

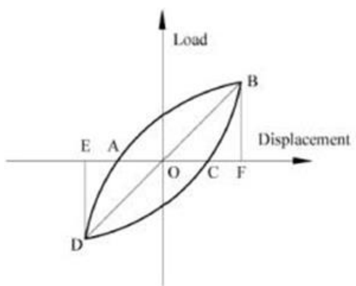


Fig. 10 Typical hysteretic loop

Table 6 Energy dissipation ratios and equivalent viscous damping ratios

| Specimens | Displacement | $E$ | $h_e$ | Specimens | Displacement | $E$ | $h_e$ |
|---|---|---|---|---|---|---|---|
| CL1 | 1Δ | 0.573 | 0.091 | CL4 | 1Δ | 0.539 | 0.086 |
| | 2Δ | 0.822 | 0.131 | | 2Δ | 0.956 | 0.152 |
| | 3Δ | 0.802 | 0.128 | | 3Δ | 0.949 | 0.151 |
| | 4Δ | 0.792 | 0.126 | | 4Δ | 1.010 | 0.161 |
| | 5Δ | 0.948 | 0.151 | | 5Δ | 0.924 | 0.147 |
| | 6Δ | 0.910 | 0.145 | | 6Δ | 0.928 | 0.148 |
| CL2 | 1Δ | 0.660 | 0.105 | CL5 | 1Δ | 0.702 | 0.112 |
| | 2Δ | 0.990 | 0.158 | | 2Δ | 0.881 | 0.140 |
| | 3Δ | 0.964 | 0.153 | | 3Δ | 0.928 | 0.148 |
| | 4Δ | 0.898 | 0.143 | | 4Δ | 0.857 | 0.137 |
| | 5Δ | 0.755 | 0.120 | | 5Δ | 0.873 | 0.139 |
| | 6Δ | 0.774 | 0.123 | | 6Δ | 0.873 | 0.139 |
| CL3 | 1Δ | 0.509 | 0.081 | CL6 | 1Δ | 0.585 | 0.093 |
| | 2Δ | 0.766 | 0.122 | | 2Δ | 0.687 | 0.109 |
| | 3Δ | 0.875 | 0.139 | | 3Δ | 0.775 | 0.123 |
| | 4Δ | 0.713 | 0.113 | | 4Δ | 0.762 | 0.121 |
| | 5Δ | 0.708 | 0.113 | | 5Δ | 0.692 | 0.110 |
| | 6Δ | NA | NA | | 6Δ | 0.683 | 0.109 |

The stiffness degradation for all cyclic loading specimens is plotted in Fig. 9, which showed that the stiffness of all specimens homogeneous decreased with the increasing displacement. This is caused by the concrete cracks and accumulated damage of studs. The ring stiffness in the positive direction was very different from its negative counterpart. This is because the small gaps between the specimen and the hydraulic loading machine, and the compression deformation of the rubber piece, so they will affect the calculated values. After this stage, the ring stiffness in the positive and negative directions at the same displacement level was close to each other. The initial stiffness increased with the increasing of stud diameter and concrete strength, but these influences decreased with the displacement increasing.

### *3.4 Energy dissipation*

In order to evaluate the actual energy dissipation ability of one hysteretic loop (see Fig. 10), energy dissipation ratio $E$ and the equivalent viscous damping ratio $h_e$ (Zhou *et al.* 2015) were calculated by Eqs. (2) and (3) to desire the energy dissipation capacity of specimens.

$$E = S_{(ABC+CDA)} / S_{(OBF+ODE)} \tag{2}$$

$$h_e = E / 2\pi \tag{3}$$

where $S_{(ABC+CDA)}$ and $S_{(OBF+ODE)}$ are the corresponding areas of the hysteretic loop in Fig. 10. The values for energy dissipation ratio $E$ and the equivalent viscous damping ratio $h_e$ is shown in Table 6 indicates that the value of $h_e$ ranged from 0.081-0.168. It can be found that the equivalent viscous damping ratio $h_e$ decreases with the stud diameter and concrete strength has limit effect on $h_e$. For example, the value of $h_e$ of specimens CL2 and CL3 decreases by 25.8% and 33.6% compared to specimen CL1 at the 5Δ. Meanwhile, the maximum difference between different

Table 7 Comparison of ultimate shear capacity in push-out and cyclic loading tests

| $d$/mm | $f_{cu}$/MPa | $P_u^+$/kN | $P_u^-$/kN | $P_u^T$/kN | $P_u^+/P_u^T$ | $P_u^-/P_u^T$ | $P_u^-/P_u^+$ |
|---|---|---|---|---|---|---|---|
| 16 | 33.1 | 85.6 | 56.9 | 81.0 | 1.057 | 0.702 | 0.665 |
| 19 | 33.1 | 116.1 | 63.5 | 104.7 | 1.109 | 0.606 | 0.547 |
| 22 | 33.1 | 121.6 | 66.6 | 116.8 | 1.041 | 0.570 | 0.548 |
| 16 | 47.8 | 94.0 | 59.3 | 103.9 | 0.905 | 0.571 | 0.631 |
| 19 | 47.8 | 111.1 | 69.9 | 120.4 | 0.923 | 0.581 | 0.629 |
| 22 | 47.8 | 146.1 | 74.4 | 155.0 | 0.943 | 0.480 | 0.509 |

specimens is less than 13% if they have the same stud diameter.

### 3.5 Ultimate shear capacity

Table 7 lists the comparison of characteristic load in push-out test and cyclic loading test. It can be found that the loading method has limit effect on the ratio of $P_u^+/P_u^T$, but has a big effect on the ratio of $P_u^-/P_u^L$. The negative ultimate shear capacity in cyclic loading test is approximately 59% of the positive ultimate shear capacity. In addition, the ratio of $P_u^+/P_u^T$ or $P_u^-/P_u^L$ of specimens with higher concrete strength is greater than that of specimens with lower concrete strength. This phenomenon mainly causes by more accumulated damage of stud.

## 4. Finite element modeling

### 4.1 General

Numerical analysis was carried out using software ABAQUS to better understand the behavior of the stud shear connectors, which is extensively adopted to the composite structures (Chang *et al*. 2014, Wang *et al.* 2012 and Nie *et al*. 2013). All components in the test, including concrete slab, headed stud shear connectors, steel beam and reinforced bars, must be properly modeled.

Eight-node reduced integral format 3D solid elements (C3D8R) with hourglass control were used to model the concrete slab, steel beam and headed stud shear connector. The reinforced bars embedded in the concrete slab used truss elements (T3D2). Fig. 11 shows the finite element (FE) mesh used to represent a quarter of the test specimen. Because of symmetry, only a quarter of the specimen arrangement is modeled. To obtain accurate results, the same mesh generations were applied on the interaction part for different components, such as the bottom of the studs and the corresponding part of the steel beam. Studs and their vicinities used the smaller mesh size of 4 mm, and the others used mesh sizes up to 20 mm.

### 4.2 Material models

The damage plasticity model of concrete and Willam-Warnke five-parameter failure criteria in ABAQUS were used for concrete in the FE modelling. The relevant parameters used for this material model are defined according to Ding *et al*. (2011) as validated by experimental results in compression and tension for concrete with strengths ranging from 20 to 140 MPa. The elastic modulus ($E_c$) and Poisson's ratio ($v_c$) are defined as 9600$f_{cu}$ N/mm$^2$ and 0.2, respectively, where $f_{cu}$ is the cubic compressive strength of concrete. Other parameter values in ABAQUS for concrete, such as dilation angle, eccentricity ratio and viscosity coefficient, were applied according to. In addition, the recovery factors of compressive and tensile stiffness, $w_c$ of 0.8 and $w_t$ of 0.2 were used as the ABAQUS default values in the calculations. The tensile damage variable ($d_t$) and compressive damage variable ($d_c$) of concrete were also calculated according to Ding *et al*. (2017).

An elastic-plastic model, considering Von Mises yielding criteria, Prandtl-Reuss flow rule, and isotropic strain hardening, was used to describe the constitutive behavior of steel. The mixed hardening model was applied for the steel. This model also accounts for the well-known Bauschinger effect for steel under cyclic loading, which is characterized by a reduced yield stress upon load reversal after plastic deformation has occurred. The elastic modulus ($E_s$) and Poisson's ratio ($v_s$) were set to 206000 N/mm$^2$ and 0.3, respectively. The yield stress at zero plastic strain was determinate by tensile test of the steel coupons, and the value of the Kinematic hard parameter ($C_1$), the change ratio of the back stress ($\gamma$), the maximum change of the yield surface ($Q_\infty$) and Hardening parameter ($b_{iso}$) was set as 7500, 50, 0.5$f_y$ and 0.1, respectively, according to Ding *et al*. (2017).

### 4.3 Boundary conditions

The symmetric boundary condition was applied to the surface at the symmetric planes of specimen, as shown in Fig. 11(a). For instance, all nodes along the middle of the steel beam web (surface 1) are restricted from moving in the $Y$ direction, i.e., the displacement of the $Y$ direction (UY), the rotation of the $X$ and $Z$ (URX, URZ) were zero due to

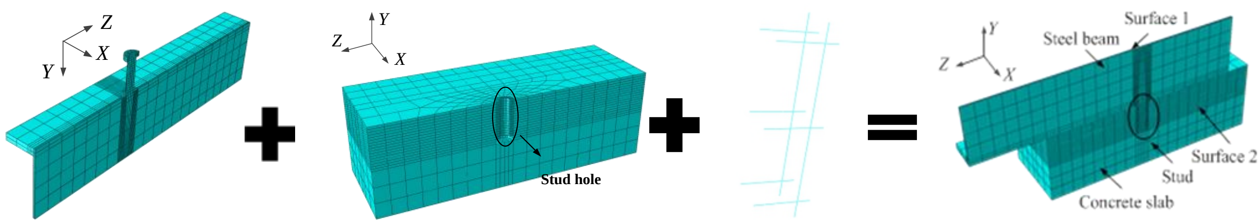


(a) Steel beam and stud (b) Concrete slab (c) Steel cage (d) Numerical model

Fig. 11 Finite element model

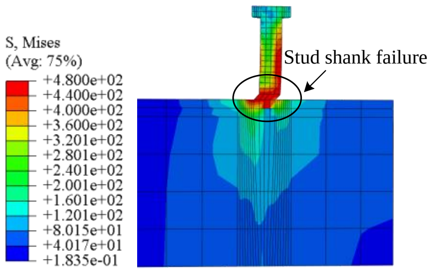


(a) Stud shank failure

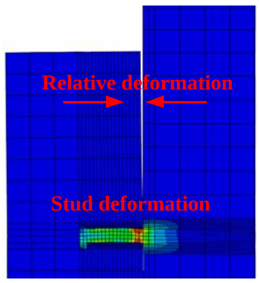


(b) Relative deformation

Fig. 12 Failure modes and Von Mises stress contours from FE results, units=MPa

symmetry. All concrete nodes, stud nodes, steel beam flange and web nodes that lie on the other symmetry surface (surface 2) are restricted from moving in the *X* direction because of symmetry as shown in Fig. 11(a), i.e., UX=URY=URZ=0. Meanwhile, the displacement of the *X*, *Y* and *Z* axis and corresponding direction rotations on the bottom of the concrete slab are fixed at the foot point.

### *4.4 Interaction and loading*

The interactions of the steel beam and concrete and the stud and concrete in the FE modeling are the most important and different part. To really reflect the behavior of studs, boolean operation is adopted to cut the concrete slabs to create a stud hole, as shown in Fig. 11(c).

The contact between the steel beam and concrete slab, and the stud and concrete slab is simulated between two matching surfaces. These two surfaces are allowed to separate from each other while penetration is not allowed. Contact in both the normal and tangential directions is defined between the flanges of the steel beam and the outer surfaces of the concrete slab. Hard contact is applied in the normal direction. The Mohr-Coulomb friction model is applied in the tangential direction and the friction coefficient is taken as 0.5 as an empirical value. Embedded constrains are also implemented to model the constraint between the concrete slab and the bars. Bond-slip between the both is neglected. The loading scheme was applied on the top surface of the steel beam according to the test.

### *4.5 Comparison and discussion of results*

The failure modes identified from the FE modeling are presented in Fig. 12. The resulting stud fracture and stud slippage and concrete failure are well supported by the experimental observations shown in Fig. 8. Figs. 5 and 6 compare the load-displacement curves and hysteretic curves from the FE and experimental results and Fig. 7 shows the skeleton load-displacement curves, both indicating a good agreement, especially for the elastic stage.

Von Mises stress contours for specimen with stud failure are shown in Fig. 12(a). It can be seen that the maximum stress of studs was 480 MPa, located at the stud bottom and exceeded the ultimate strength (approximately 480 MPa) of the stud, leading to the failure of the stud, consistent with the experimental results (Fig. 8(a)). However, the maximum von Mises stress in the steel beam was small (less than 280 MPa, still within the elastic stage) in comparison to the steel yield strength (313.1 MPa). The stud displacement and corresponding von Mises stress decreased gradually from the bottom to the top. Meanwhile, the relative slippage can be caught from the FE results due to the distortion of the stud.

## 5. Simplified model of *P*-Δ hysteretic relationship

### *5.1 Simplified skeleton curve model*

The strength of stud and the concrete strength are the main factors affecting the behavior of shear connectors according to references (Zhu *et al*. 2016, Hu *et al*. 2016). It is necessary to determine several key parameters before obtaining the calculation formula of the skeleton curve, such as positive ($P_u^+$) and negative ($P_u^-$) ultimate shear capacity and the corresponding displacement ($\Delta_0^+$ and $\Delta_0^-$), positive ($G_s^+$) and negative ($G_s^-$) elastic stiffness.

#### *5.1.1 Ultimate shear capacity*

The expressions of the ultimate shear capacity in bi-direction push-out test have been presented in the former paper. In this investigation, FE models with stud diameter ranging from 16 mm to 27 mm and with concrete strength ranging from 20 MPa to 100 MPa have been done to investigate the relationship of the ultimate shear capacity between cyclic loading test ($P_u^+$ and $P_u^-$) and bi-direction push-out test ($P_u^T$ and $P_u^L$). It was found that the concrete strength and stud diameter have limit effect on the ultimate displacement for cyclic loading specimens by means of FE analyses, and the ultimate displacement of stud specimens in positive ($\Delta_0^+$) and negative ($\Delta_0^-$) direction was approximately 1.5 mm and 2.0 mm, respectively. Fig. 13(a) and 13(b) show the relationship curve of the ratio of $P_u^+/P_u^T$ and concrete strength $f_{cu}$, and the ratio of $P_u^-/P_u^L$ and $f_{cu}$, respectively. Based on the test and FE results, regression analysis method is taken and the expressions for $P_u^+$ and $P_u^-$ can be obtained as

$$P_u^+ = (1.05 - 0.0045 f_{cu}) P_u^T \tag{4}$$

$$P_u^- = 0.8 P_u^L = \frac{0.8 P_u^T}{(1 + 0.003 f_{cu})(0.7 + 0.03d)(0.24 + 0.002 f_s)} \tag{5}$$

$$P_u^T = (0.2d^{1.7} - 10) f_{cu}^{\,0.8 - 0.15\ln(d-10)} (0.002 f_s + 0.24) \tag{6}$$

$$P_u^L = \frac{(0.2d^{1.7} - 10) f_{cu}^{\,0.8 - 0.15\ln(d-10)}}{(1 + 0.003 f_{cu})(0.7 + 0.03d)}$$

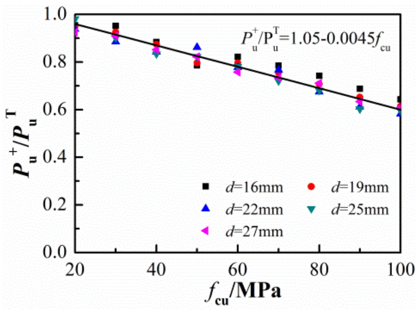


(a) $P_u^+/P_u^T$

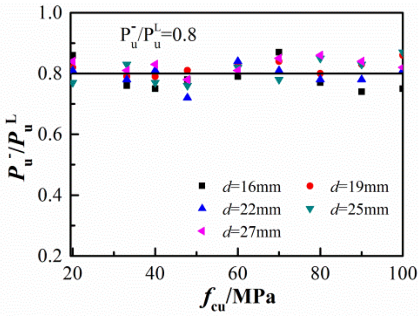


(b) $P_u^-/P_u^L$

Fig. 13 Ratio of ultimate shear capacity

$$= \frac{P_u^T}{(1+0.003 f_{cu})(0.7+0.03d)(0.24+0.002 f_s)} \tag{7}$$

where $P_u^T$ is the ultimate shear capacity of a single stud in push-out test; $f_{cu}$ is the cubic compressive strength of concrete; $f_s$ is the stud yield strength and $d$ is the diameter of stud shank.

*5.1.2 Elastic stiffness*

The bond stiffness $G_s^+$ and $G_s^-$ are defined as the secant modulus according to 40% of the positive and negative ultimate shear capacity, respectively and determined by regression analysis as

$$G_s^+ = \frac{3(d-7)}{0.7d-3} P_u^+ \tag{8}$$

$$G_s^- = \frac{3d-6}{0.7d-6} P_u^- \tag{9}$$

The variables $A_5$ and $A_6$ are defined as the ratio of positive elastic stiffness ($G_s^+$) to peak secant stiffness $G_0^+$ ($G_0^+=P_u^+/\Delta_0^+$), and negative elastic stiffness ($G_s^-$) to peak secant stiffness $G_0^-$ ($G_0^-=P_u^-/\Delta_0^-$), respectively, which can be expressed as

$$A_5 = \frac{G_s^+}{G_0^+} = \left[\frac{3(d-7)}{0.7d-3} P_u^+\right] / \left(\frac{P_u^+}{1.5}\right) = \frac{45d-315}{7d-30} \tag{10}$$

$$A_6 = \frac{G_s^-}{G_0^-} = \frac{(3d-6)P_u^- / (0.7d-5)}{P_u^- / 2} = \frac{40d-120}{7d-50} \tag{11}$$

*5.1.3 Calculation formula of skeleton curve*

Therefore, the following calculation formula of skeleton curve is proposed based on the above key parameters

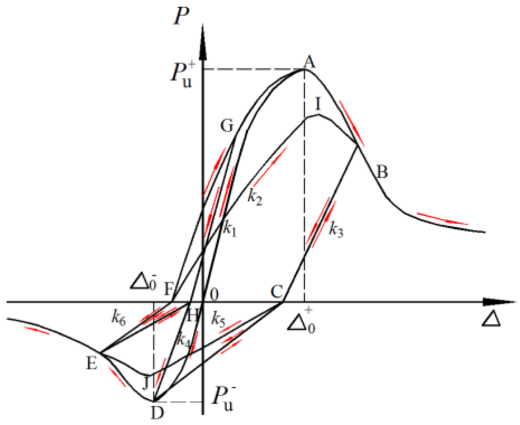


Fig. 14 Simplified hysteretic model

$$y = \begin{cases} \dfrac{A_7 + (B_7 - 1)x^2}{1 + (A_7 - 2)x + B_7 x^2} & x \le 1 \\ \dfrac{x}{\alpha_7 (x-1)^2 + x} & x > 1 \end{cases} \tag{12}$$

where $y$ is the ratio of load to ultimate shear capacity, defined as $y=P/P_u$, and $P_u=P_u^+$ or $P_u^-$. $x$ is the ratio of the corresponding displacement, defined as $x=\Delta/\Delta_u$; $B_7$ is a parameter with the value of $1.6(A_7-1)^2$, and $A_7=A_5$ or $A_6$; the variable $\alpha_7$ is equal to 0.15.

Comparisons between the skeleton curves predicted by theoretic calculation formula Eq. (12) and the experimental curves are shown in Fig. 7. The proposed expression gives a good estimate of stud shear connectors under cyclic loading.

*5.2 Simplified hysteretic rule of load P versus displacement Δ relationship*

Because of the accumulated damages in the specimens under cyclic loading, the stiffness of the test specimens decreased from one cycle to the next displacement level. So, the hysteretic curve was simplified into a hybrid model consisting of straight and curve segments, as shown in Fig. 14.

*5.2.1 Positive loading and unloading segment*

The decreased coefficient of rigidity in the positive loading and unloading process was determined by regression analysis (see Fig. 15) based on both experimental and numerical results, and the corresponding results can be expressed as

$$k_2=m_1k_1 \tag{13}$$

$$k_3=m_2k_1 \tag{14}$$

$$m_1=2(\Delta/\Delta_y^+)^{-1.1} \tag{15}$$

$$m_2=(\Delta_u/\Delta_y^+)^{-0.8} \tag{16}$$

where $k_1$ is the initial elastic stiffness and measured by MPa, equal to the positive bond stiffness $G_s^+$; $k_2$ and $k_3$ is the positive loading and unloading stiffness, respectively, and $m_1$ and $m_2$ are the corresponding decreased coefficient of rigidity; $\Delta_y^+$ is the positive yield displacement.

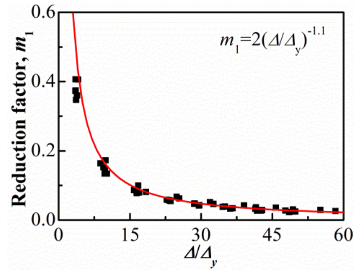


(a) Reduction factor $m_1$

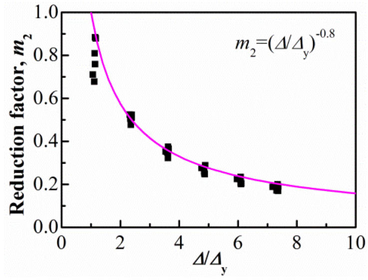


(b) Reduction factor $m_2$

Fig. 15 Reduction factor of positive stiffness

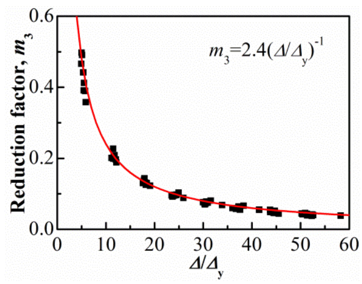


(a) Reduction factor $m_3$

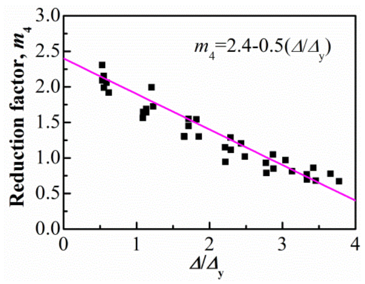


(b) Reduction factor $m_4$

Fig. 16 Reduction factor of negative stiffness

### 5.2.2 Negative loading and unloading segment

The decreased coefficient of rigidity in the negative loading and unloading process was also determined by regression analysis (see Fig. 16) based on experimental and numerical results, and the corresponding results can be expressed as

$$k_5=m_3k_4 \tag{17}$$

$$k_6=m_4k_4 \tag{18}$$

$$m_3=2.4(\Delta/\Delta_y^-)^{-1} \tag{19}$$

$$m_4=2.4-0.5(\Delta/\Delta_y^-) \tag{20}$$

where $k_4$ is the negative initial elastic stiffness and measured by MPa, equal to the negative bond stiffness $G_s^-$; $k_5$ and $k_6$ are the negative loading and unloading stiffness, respectively, and $m_3$ and $m_4$ are the corresponding decreased coefficient of rigidity; $\Delta_y^-$ is the negative yield displacement.

### 5.2.3 Simplified hysteretic rule

The simplified hysteretic load ($P$) versus displacement ($\Delta$) relationship of studs (see Fig. 14), is modified to simulate the seismic behavior of studs, i.e., using the model parameters obtained from the above-mentioned. The simplified hysteretic curve can be divided into five stages as following: elastic stage, elastic-plastic stage, unloading stage, elastic-plastic stage of reverse loading, descending stage. The step to calculate the $P$-Δ hysteretic curve based on the simplified model can be summarized as follows:

(1) To calculate the values of $P_u^+$, $P_u^-$, $\Delta_0^+$, $\Delta_0^-$, $G_s^+$, $G_s^-$, and the corresponding stiffness reduction factor according to Eqs. (4)-(20);

(2) In the positive loading stage, if the displacement is less than $\Delta_y^+$, the corresponding load $P$ was determined according to the linear relation, and the positive bond stiffness $G_s^+$ (equal to $k_1$) were taken as the initial stiffness, and the unloading stiffness $k_3$ were used to determine the load $P$, such as from point B to C. In the inverse loading stage, if the displacement is less than $\Delta_y^-$, the negative bond stiffness $G_s^-$ (equal to $k_4$) was applied as the initial stiffness and the corresponding unloading stiffness $k_6$ was used to calculate the load. In the subsequent cycle, the loading stiffness $k_2$ and $k_5$ were taken as the positive and negative loading stiffness, respectively.

(3) If the former displacement increment is positive, it means the loading stage. Otherwise it means the unloading stage. The load $P$ is calculated by corresponding loading or unloading stages.

(4) Repeat the step (2)-(4) until the displacement reaches its desired value.

To verify the simplified model, the predicted $P$-Δ hysteretic relationships using the simplified model are compared with experimental curves, as shown in Fig. 17. It can be found that from the comparison that, general, a reasonable agreement is achieved.

## 6. Conclusions

The seismic behavior of headed stud shear connector was investigated through experimental studies and FE analysis. Six push-out tests and twelve cyclic loading tests were carried out. The accuracy and reliability of the numerical analysis was verified. The design formulas for expressing the skeleton curve were proposed and the corresponding hysteretic model of load versus displacement was then established. The following conclusions can be made based on the tests and FE analysis.

- The experimental results demonstrated that stud failure and concrete failure are the typical failure modes in both of the push-out tests and cyclic loading tests. The ultimate shear capacity per stud increased with the stud diameter and yield strength of studs. For cyclic loading specimens, all of the hysteresis curves were full and basically appeared to be reversed S shape with obvious

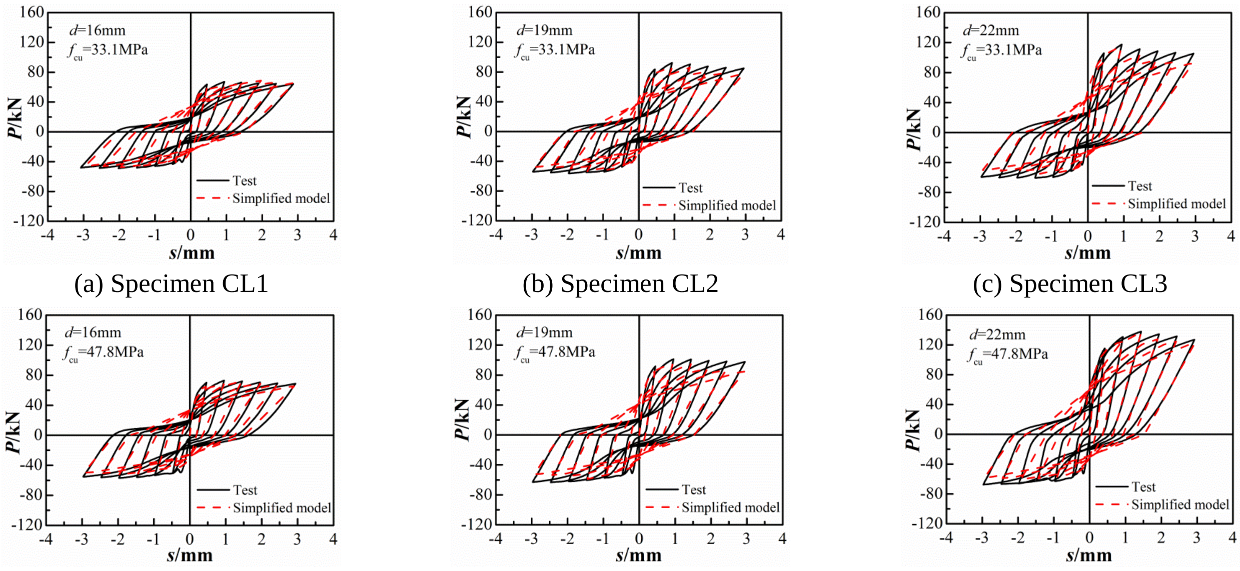


(a) Specimen CL1 (b) Specimen CL2 (c) Specimen CL3

(d) Specimen CL4 (e) Specimen CL5 (f) Specimen CL6

Fig. 17 Comparison of *P* versus Δ relationships between simplified model and test results

pinching phenomenon. The stiffness of all specimens homogeneously decreased with the increasing of displacement. The value of equivalent viscous damping ratio $h_e$ ranged from 0.081 to 0.168, which indicated a good energy dissipation capacity and $h_e$ decreased with the stud diameter.

• An accurate finite element model was developed and relevant calculated parameters in the FE analysis were suggested. The developed numerical model gave satisfactory and efficient simulation of the behavior and ultimate shear capacity of stud in push-off and cyclic loading tests. It is therefore recommended to be used for the structural design and analysis in practice.

• Based on the experimental and numerical results, design formulas for calculating the skeleton curve were proposed and the corresponding simplified hysteretic model of load versus displacement was then established. It is demonstrated that the proposed formulas and simplified hysteretic model have a better match with the test results.

## Acknowledgments

This research work was financially supported by the National Natural Science Foundation of China (Grant No. 51578548), the National Key R&D Plan of China (Grant No. 2017YFC0703400), the Fundamental Research Funds for the Central Universities of Central South University (Grant No. 2016zzts071) and the Hunan Provincial Innovation Foundation for Postgraduate (Grant No. CX2017B059). The financial support is highly appreciated.

## References

BS 5400-5 (1979), Steel, Concrete and Composite Bridges, Part 5: Code of Practice for Design of Composite Bridges, British Standard Institution, London, Britain.

Chang, X., Luo, X.L, Zhu, C.X. and Tang, C.A. (2014), "Analysis of circular concrete-filled steel tube support in high ground stress conditions", *Tunnel. Underg. Space Technol.*, **43**(3), 41-48.

Debski, H., Teter, A., Kubiak, T. and Samborski, S. (2016), "Local buckling, post-buckling and collapse of thin-walled channel section composite columns subjected to quasi-static compression", *Compos. Struct.*, **136**, 593-601.

Ding, F.X., Yin, G.A., Wang, L.P., Hu, D. and Chen, G.Q. (2017), "Seismic performance of a non-through-core concrete between concrete-filled steel tubular columns and reinforced concrete beams", *Thin Wall. Struct.*, **110**, 14-26.

Ding, F.X., Ying, X.Y., Zhou, L.C. and Yu, Z.W. (2011), "Unified calculation method and its application in determining the uniaxial mechanical properties of concrete", *Front. Arch. Civil Eng.*, **5**(3), 381-393.

EN 1994-1-2 (2004), Design of composite steel and concrete structures, Part 1.1: General rules and rules for buildings-General rules, European Committee for Standardization; Brussels, Brussels.

Fang, G.S., Wang, J.Q., Li, S. and Zhang, S.B. (2016), "Dynamic characteristics analysis of partial-interaction composite continuous beams", *Steel Compos. Struct.*, **21**(1), 195-216.

Gattesco, N. and Giuriani, E. (1996), "Experimental study on stud shear connectors subjected to cyclic loading", *J. Constr. Steel Res.*, **38** (1), 1-21.

GB/T 228-2010 (2010), Metallic materials-Tensile testing at ambient temperature, Ministry of Housing and Urban-Rural Development of the People's Republic of China; Beijing, China.

GB/T 50081-2016 (2016), Standard for test method of mechanical properties on ordinary concrete, Ministry of Housing and Urban-Rural Development of the People's Republic of China; Beijing, China.

Hanswille, G., Porsch, M. and Ustundag, C. (2007a). "Resistance of headed studs subjected to fatigue loading: Part I: Experimental study", *J. Constr. Steel Res.*, **63**(4), 475-484.

Hanswille, G., Porsch, M. and Ustundag, C. (2007b). "Resistance of headed studs subjected to fatigue loading: Part II: Analytical study", *J. Constr. Steel Res.*, **63**(4), 485-493.

Hu, H.S., Nie, J.G. and Wang, Y.H. (2016), "Shear capacity of concrete-filled steel plate composite coupling beams", *J. Constr.*

*Steel Res*., **118**, 76-90.

Ju, X.C. and Zeng, Z.B. (2015), "Study on uplift performance of stud connector in steel-concrete composite structures", *Steel Compos. Struct.*, **18**(5), 1279-1290.

Liu, J., Ding, F.X., Liu, X.M. and Yu, Z.W. (2016), "Study on flexural capacity of simply supported steel-concrete composite beam", *Steel Compos. Struct.*, **21**(4), 829-847.

Nie, J.G., Wang, Y.H. and Cai, C.S. (2011), "Experimental Research on fatigue behavior of RC beams strengthened with steel plate-concrete composite technique", *J. Struct. Eng.*, **137**(7), 772-781.

Prakash, A., Anandavalli, N., Madheswaran, C.K. and Lakshmanan, N. (2012), "Experimental investigation on flexural behaviour of HSS stud connected steel-concrete composite girders", *Steel Compos. Struct*., **13**(3), 239-258.

Uy, B. (2003), "High-strength steel-concrete composite columns for buildings", *Proceedings of the Institution of Civil Engineers - Structures and Buildings*, **156**(1), 3-14.

Wang, B., Huang, Q. and Liu, X.L. (2017), "Deterioration in strength of studs based on two-parameter fatigue failure criterion", *Steel Compos. Struct.*, **23**(2), 239-250.

Wang, Y.H., Nie, J.G. and Cai, C.S. (2013), "Numerical modeling on concrete structures and steel-concrete composite frame structures", *Compos. Part B: Eng.*, **51**(8), 58-67.

Wang, Y.H., Nie, J.G. and Li, J.J. (2014), "Study on fatigue property of steel-concrete composite beams and studs", *J. Constr. Steel Res.*, **94**(94), 1-10.

Wiese, S., Schnell, J. and Kurz, W. (2011), "Innovative shear connectors in ultra high performance concrete", *Beton-und Stahlbetonbau*, **106**(10), 694-699.

Zhou, T., Jia, Y.M., Xu, M.Y., Wang, X.D. and Chen, Z.H. (2015), "Experimental study on the seismic performance of L-shaped column composed of concrete-filled steel tubes frame structures", *J. Constr. Steel Res.*, **114**, 77-88.

Zhu, Z.H., Zhang, L., Bai, Y., Ding, F.X., Liu, J. and Zhou, Z. (2016), "Mechanical performance of shear studs and application in steel-concrete composite beams", *J. Centeral South Univ.*, **23**(10), 2676-2687.

*BU*